



From Salar to Cells: Validating Brine-Sourced Li_2CO_3 from Salar de Uyuni for Lithium-Ion Battery Cell Manufacture

Satish Bolloju* , Edgar Bautista Quisbert, Gerard Bree, Gaurav C. Pandey, Galo J. Páez Fajardo , Matthew J. W. Ogley, Ashok S. Menon, Paola Patiño Gutiérrez, Danitza Delgado Bobarin, Sanghamitra Moharana, Muhammad Ans, Eleni Fiamégkou, Rebecca A. Sellers, and Louis F. J. Piper*

In this study, lithium carbonate (Li_2CO_3) sourced from the Salar de Uyuni salt flat in Bolivia was used in the synthesis of cathode active material for Li-ion batteries. X-ray diffraction, atomic absorption spectrometry, and scanning electron microscopy analyses confirmed that the material had a high phase purity (99.59%, battery-grade) and a suitable morphology for active material synthesis, comparable to a similar commercially obtained material. $\text{Li}[\text{Ni}_{1/3}\text{Mn}_{1/3}\text{Co}_{1/3}]\text{O}_2$ (NMC111) was synthesized as a model system using Li_2CO_3 as the precursor and evaluated in full, large-format pouch cells along with three-electrode cells, using commercially relevant active material fractions and mass loadings for meaningful assessment of electrochemical performance. These cells exhibited capacities close to theoretical values and similar to that of commercially obtained NMC111, demonstrating the viability of the raw material. Operando X-ray diffraction analysis of aged pouch cells revealed that capacity loss was due to depletion of lithium inventory, without any disruption to the long-range cathode crystal structure or significant degradation in lithium kinetics. Postmortem analysis of the cycled electrodes further confirmed that transition metal dissolution and lithium trapping on the anode side were key contributors to the capacity fading observed in the pouch cells. This work demonstrates the potential of Salar de Uyuni's lithium resources for the production of cells relevant to practical applications.

1. Introduction

Lithium-ion batteries (LIBs) have revolutionized modern portable electronics and electric transportation through their superior performance

Dr. S. Bolloju, Dr. G. Bree, Dr. G. C. Pandey, Dr. G. J. Páez Fajardo, M. J. W. Ogley, Dr. A. S. Menon, Dr. S. Moharana, M. Ans, Dr. E. Fiamégkou, R. A. Sellers, Prof. L. F. J. Piper

WMC, University of Warwick, Coventry CV4 7AL, UK

E-mail: satish.bolloju@warwick.ac.uk

E-mail: louis.piper@warwick.ac.uk


Dr. E. Bautista Quisbert, P. Patiño Gutiérrez, D. D. Bobarin

Planta Piloto de Materiales Catódicos, YLB, S/N a 17 km de Potosí, La Palca, Potosí, Bolivia

Dr. G. Bree, Dr. G. J. Páez Fajardo, M. J. W. Ogley, Dr. A. S. Menon, M. Ans,

Dr. E. Fiamégkou, Prof. L. F. J. Piper

The Faraday Institution, Quad One, Harwell Campus, Didcot OX11 0RA, UK

 The ORCID identification number(s) for the author(s) of this article can be found under <https://doi.org/10.1002/eam2.70053>.

DOI: 10.1002/eam2.70053

and widespread adoption.^[1] The ongoing rapid increase in the production of electric vehicles (averaging 47% year on year growth from 2015 to 2022) has resulted in high demand for raw materials, particularly lithium, which is now considered a “critical” material by the European Commission (EU)^[2] and United States Department of Energy (US DOE).^[3] Global lithium production tripled between 2010 and 2020;^[4] however, the demand is projected to increase by as much as 40-fold by 2050.^[5] The global lithium supply chain for LIBs faces major challenges due to its non-uniform distribution across the world, and the rapid growth in demand requires new lithium sources to address supply chain vulnerability.^[6] Lithium is typically extracted and processed into lithium carbonate (Li_2CO_3), lithium oxide, or hydroxide from hard rock or brine sources. Brine-based production offers significantly lower greenhouse gas emissions compared to hard rock mining.^[7] This difference is attributed to the higher energy consumption of the excavation and refining processes associated with hard rock lithium.^[8]

Salar de Uyuni, located in southwest Bolivia, harbors one of the world's largest lithium brine resources, estimated at 23 million metric tons.^[9,10] This makes Salar de Uyuni a hot spot for global lithium extraction efforts, providing a key raw material for the burgeoning battery industry.^[11] Developing new lithium sources, such as Salar de Uyuni, offers a pathway to diversifying and stabilizing the global lithium supply, while also addressing concerns about environmental sustainability. Several studies have investigated the production of Li_2CO_3 from brines sourced from various locations. For instance, An et al.^[12] developed a hydrometallurgical technique to recover lithium from brine sourced from the Salar de Uyuni, achieving a purity of 99.55%, along with other valuable by-products. In another study, a two-stage Li_2CO_3 precipitation process was designed to eliminate impurities and enhance lithium recovery from brine obtained from the Damxungcuo saline lake in Tibet, which proved to be highly effective for the production of battery-grade Li_2CO_3 .^[13] More recently, Li_2CO_3 obtained from brine was used in the synthesis of lithium bis(oxalate) borate (LiBOB), which was employed as an additive in carbonate-based electrolyte for NMC/Li cells.^[14] While these studies focused primarily

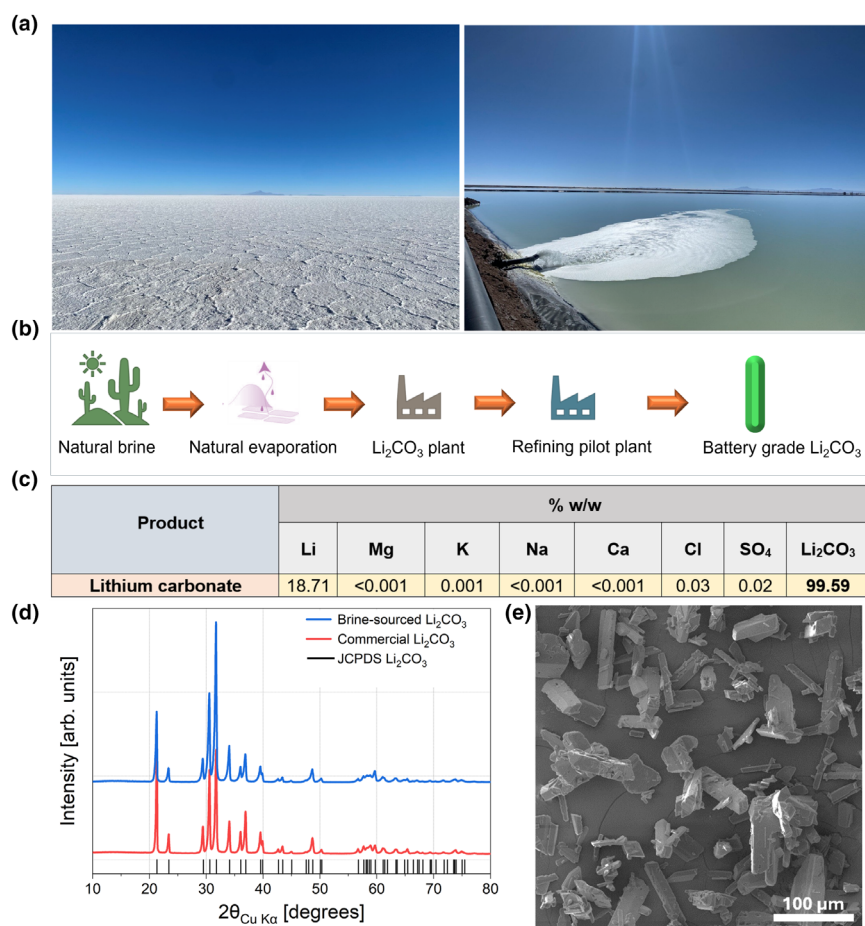


Figure 1. a) Uyuni salt flat in Bolivia (left) and salt brine pumped into evaporation pond (right). b) Schematic representation of the extraction and purification of Li₂CO₃ from brine. c) Elemental composition of brine-sourced Li₂CO₃ from AAS. d) XRD patterns of brine-sourced and commercial Li₂CO₃ powders. e) SEM image of brine-sourced Li₂CO₃ powder.

on improving the Li₂CO₃ production process, they did not specifically address its direct application in lithium-ion battery cathode synthesis.

The extracted lithium precursor is refined to ensure quality and suitability for battery applications and can be used as a reactant in the synthesis of cathode active materials such as NMC111 and lithium iron phosphate, through methods like co-precipitation, combustion, sol-gel, hydrothermal, and solid-state techniques. Within synthesis, the purity of the feedstock is critical in achieving high-performance batteries.^[15]

Cathode materials that offer high energy densities, adequate safety, and stable cycling are crucial for the battery community; Li[Ni_xMn_yCo_z]O₂ ($x + y + z = 1$) meets these criteria. In particular, Li[Ni_{1/3}Mn_{1/3}Co_{1/3}]O₂ (NMC111) offers distinct advantages over other Ni-rich chemistries, such as enhanced thermal abuse tolerance,^[16] improved capacity retention,^[17] and reduced sensitivity to moisture and air;^[18] therefore, it is widely investigated and commercially adopted. NMC111 exhibits a reversible specific capacity of ~160 mAh g⁻¹ in a voltage range of 2.5–4.2 V (vs graphite).^[19] Co-precipitation is particularly advantageous for the synthesis of NMC111 due to its scalability, cost-effectiveness, ease, homogenous atomic-level mixing, and precise control over the particle morphology.^[20]

An accurate assessment of the electrochemical performance of the synthesized NMC111 is crucial for validating the potential of Li₂CO₃ coming from the Salar for commercial applications. Several studies have evaluated the electrochemical performance of synthesized NMC111 materials using half-coin cells; however, this approach has intrinsic design limitations, which can lead to potential inaccuracies in evaluating material behavior.^[21] Specifically, the use of excess electrolyte, a low active material percentage, and/or low mass loading, and a large reservoir of Li inventory in half-coin cells can obscure the true electrochemical dynamics of the material, such as electrolyte decomposition, lithium inventory loss, and side reactions, which significantly affect battery life and efficiency.^[22] Therefore, half-coin cell testing may not always be a true representation of the electrochemical performance observed in industrially relevant full cell formats,^[21] and meaningful validation requires scaling up the synthesis to enable fabrication of full and larger cell formats.

Herein, Li₂CO₃ sourced from the rich reserves of Salar de Uyuni, Bolivia, was purified to achieve battery-grade quality. The obtained Li₂CO₃ was thoroughly characterized before utilization as a lithium precursor for production of NMC111 cathode material to validate its potential for the synthesis of battery cathode materials. Unlike previous research on brine-sourced Li₂CO₃, which has predominantly focused on its production processes, our study utilized this material in cathode synthesis to demonstrate its potential for practical applications. We evaluated the electrochemical performance of the synthesized NMC111 in both

three-electrode (3E) and larger-area pouch cells, providing a more accurate and realistic assessment of its electrochemical behavior. Additionally, we investigated the capacity fading mechanism of NMC111 by performing long-duration operando XRD on large-format pouch cells, without compromising the integrity of the cell format. This approach offers valuable insights into the real-world performance and degradation processes of the material.

2. Results and Discussion

Figure 1a shows Bolivia's Uyuni salt flat and brine being pumped into an evaporation pond. A schematic of the extraction and purification process of Li₂CO₃ from the brine is shown in Figure 1b, and the detailed extraction and purification processes are described in the experimental section. Firstly, Li₂CO₃ was characterized and compared with commercial battery-grade Li₂CO₃ using powder XRD. Additional characterization of the brine-sourced Li₂CO₃ was performed using SEM and atomic absorption spectrometry (AAS). The purity of the extracted Li₂CO₃ was determined to be 99.59% from AAS measurements; this indicates that the material is of battery grade (Figure 1c).^[23,24] A high

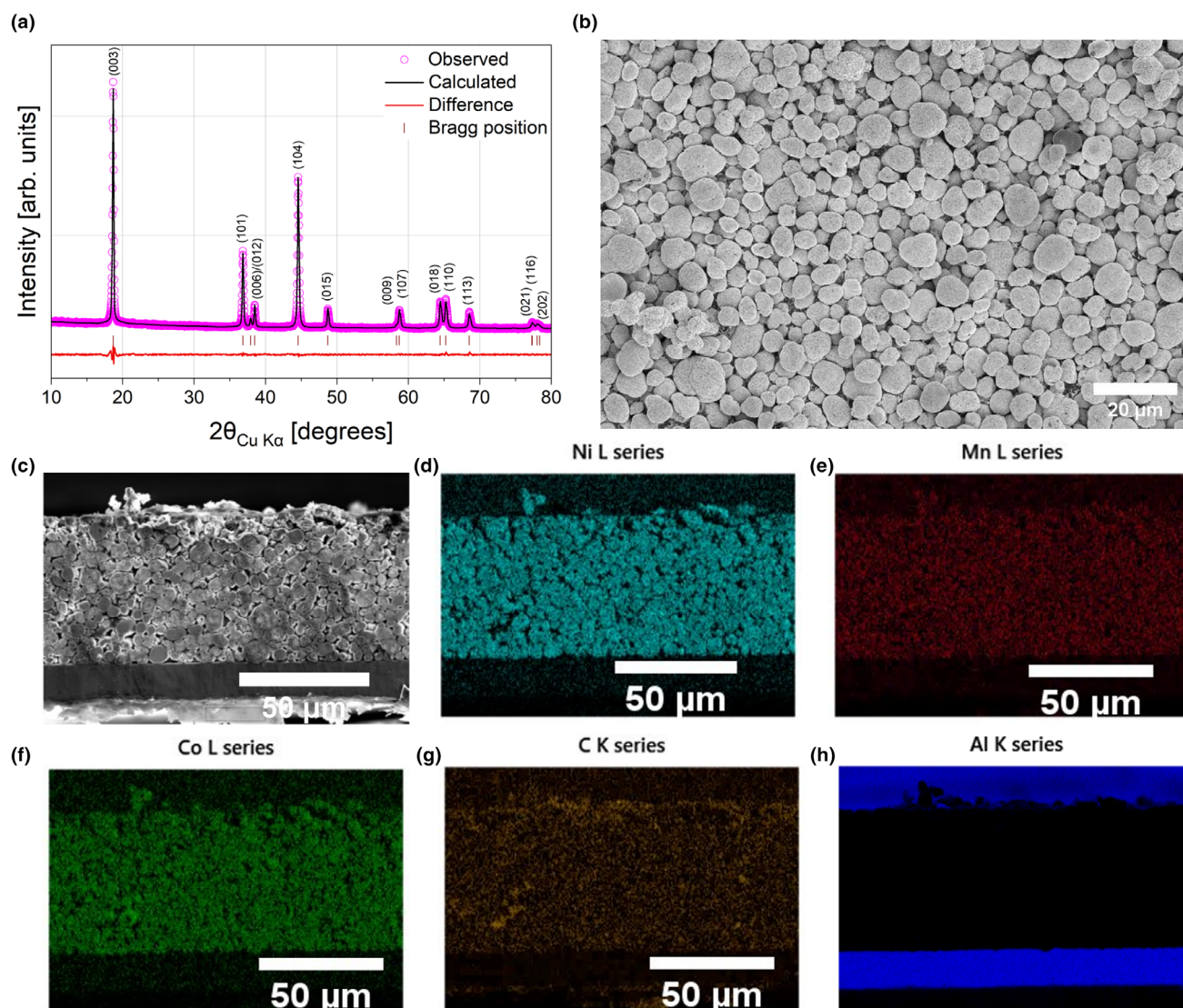


Figure 2. a) Rietveld refinement data of XRD pattern for NMC111. b) SEM image of NMC111 powder. c) Cross-sectional SEM image coupled with d–h) EDS mapping of NMC111 electrode.

feedstock purity is critical for good battery performance. The XRD pattern indicates that the brine-sourced Li_2CO_3 material did not contain crystalline impurities, based on the standard Li_2CO_3 (JCPDS #00-022-1141), and it matched well with that of commercial Li_2CO_3 (Figure 1d). The SEM micrographs show an elongated rectangular structure for Li_2CO_3 (Figure 1e), matching the morphology of commercial Li_2CO_3 .^[25]

To further validate the brine-sourced Li_2CO_3 material for Li-ion battery applications, NMC111 was synthesized using a co-precipitation method and Li_2CO_3 as the lithium precursor, and its structural and electrochemical properties were investigated. The XRD pattern and its representative refinement data for the synthesized NMC111 are shown in Figure 2a. A characteristic diffraction pattern of phase-pure NMC (JCPDS #44-0145) without any secondary phases was observed; the pattern showed sharp peaks, indicating a high degree of crystallinity. NMC exhibits a typical layered $\alpha\text{-NaFeO}_2$ structure. The XRD peaks can

be indexed to the $R\bar{3}m$ space group. Refinement was used to calculate the structural parameters of the material, and the lattice parameters a and c were found to be 2.85802(3) and 14.2275(4) Å, respectively, consistent with earlier reports.^[26] The crystallographic data of the Rietveld refinement is shown in Table S1, Supporting Information. Refinement of the powder diffraction data enabled us to semi-quantitatively determine the degree of cation mixing in the cathodes. Based on the refinement data, the Li/Ni intersite mixing ratio was calculated to be 2.9%, which is below the critical threshold of 4%.^[27] Lower intersite mixing reduces anisotropic stress in the bulk, which can otherwise lead to mechanical degradation and capacity fading.^[28–30] The obvious splitting of the (006)/(012) and (018)/(110) planes indicated the formation of a well-defined hexagonal lattice structure. The c/a ratio of 4.98 indicated a good hexagonal structure of the material.^[31] The integrated intensity ratio of the (003)/(104) peaks ($I(003)/I(104)$) was 1.28, indicating lower cation mixing, corroborating the refinement results.

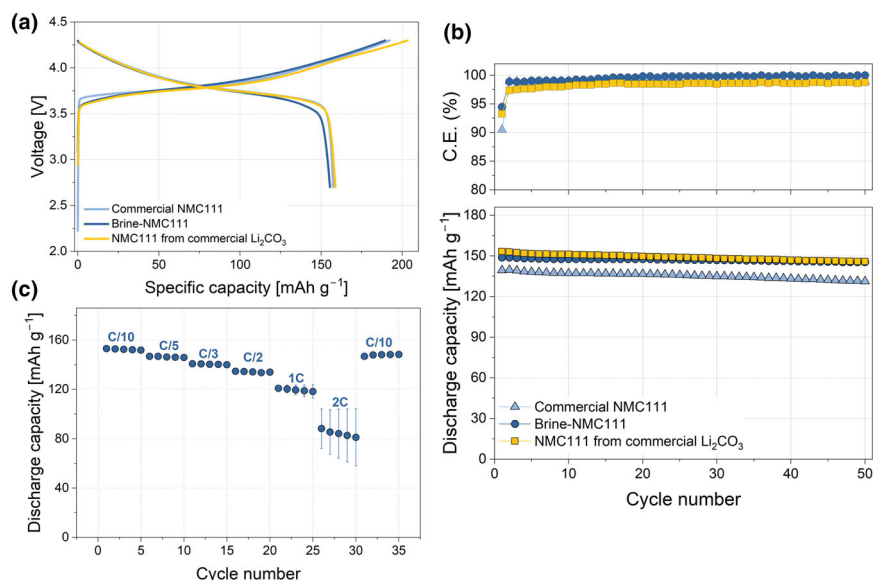


Figure 3. a) First cycle charge/discharge voltage profiles at C/10, cycled between 2.7 and 4.3 V. b) Cycle life and CE at 1 C. c) Rate capability of brine-NMC111.

An I(003)/I(104) value lower than 1.2 results in undesirable cation mixing and poor electrochemical performance of the material.^[32] The XRD pattern of commercially sourced NMC111 powder is shown in Figure S1, Supporting Information for comparison. The morphology and particle size distributions of NMC material synthesized using brine-sourced Li_2CO_3 (hereafter referred to as brine-NMC111) was compared with that of commercial NMC111. The brine-NMC111 revealed secondary particles with a spherical morphology with diameters ranging between 2 and 10 μm (Figure 2b) and an average particle size of 5 μm (Figure S2, Supporting Information). Particle size distribution measurements confirmed this, indicating a median particle size (Dv50) of 6.78 μm , with a distribution range of 4.26 μm (Dv10) to 11.0 μm (Dv90) (Figure S3a, Supporting Information). Commercial NMC111 exhibited a wider particle size distribution, with Dv10, Dv50, and Dv90 values of 6.52, 12, and 20.7 μm , respectively (Figure S3b, Supporting Information). These differences in particle sizes likely originate from different synthesis conditions; however, a narrow particle size distribution is usually preferred for better electrochemical performance.^[33,34] The tap density of the brine NMC111 powder was measured to be 2.1 g cm^{-3} . Furthermore, X-ray fluorescence (XRF) was used to determine the elemental composition of the synthesized material. The molar ratios of Ni, Co, and Mn were 0.307, 0.329, and

0.365 mol respectively, which were close to the desired values (Figure S4, Supporting Information). These results indicate the successful synthesis of NMC111 with desirable properties. EDS mapping of the cross-sectioned NMC111 electrode showed a uniform distribution of Ni, Co, Mn, and carbon (Figure 2c–h). A proper distribution of carbon is essential for good conductivity of the electrode during cycling.^[35] The atomic ratio of Ni, Co, and Mn in the EDS spectrum of the cross-sectioned electrode was approximately 1:1:1 (Figure S5, Supporting Information).

The electrochemical performance of the brine-NMC111 was compared with those of commercial NMC111 and NMC111 synthesized using commercial Li_2CO_3 . All samples were tested in a similar half-cell (NMC vs Li) format with low mass loadings to mimic academic studies. The first formation cycle voltage profiles of all three materials showed similar specific charge and discharge capacities (Figure 3a). The first cycle discharge capacities of brine-NMC, NMC synthesized using commercial

Li_2CO_3 , and commercial NMC111 were 155.4, 158.8, and 157.4 mAh g^{-1} , respectively, with corresponding Coulombic efficiencies (CEs) of 82.1%, 78.1%, and 81.8%. After 50 cycles, the capacity retentions were 98% for brine-NMC, 95% for NMC from commercial Li_2CO_3 , and 94% for commercial NMC111 (Figure 3b). Notably, the capacity retention and average CE of brine-NMC were higher than those of other materials. The electrochemical performance was comparable to that of materials synthesized using the co-precipitation method (see Table 1). This further confirmed the high quality of feedstock Li_2CO_3 , as high levels of impurities could negatively impact cycle life.^[40] However, it should be noted that the low mass loadings of these electrodes may obscure potential issues such as poor electrolyte wetting and longer electrical and lithium-ion diffusion pathways associated with thick electrodes.^[41]

Three half-coin cells were assembled for the brine-NMC for C-rate and statistical measurements. Here, higher mass loading (18 mg cm^{-2}) electrodes were used to gain more meaningful data on real-world performance. The cells demonstrated average discharge specific capacities of 153, 147, 141, 134, 120, and 84 mAh g^{-1} at C/10, C/5, C/3, C/2, 1 C, and 2 C, respectively. When the C-rate returned to C/10, the cells retained most of their initial capacities (Figure 3c). The decrease in capacity at higher C-rates reflects the kinetic limitations inherent to

Table 1. Summary of NMC111 materials synthesized via co-precipitation and their electrochemical characteristics.

System	Mass loading (mg cm^{-2})	Formulation	Voltage	Retention	Ref.
NMC111/Li	3–4	80:10:10	3–4.3	>60% retention after 100 cycles at 1 C	[36]
	7	80:10:10	2.5–4.3	95% retention after 50 cycles at 1 C	[20]
	4–5	80:13:7	2.7–4.3	96% after 100 cycles at 1 C	[37]
	Not provided	80:10:10	2.8–4.3	96.6% after 50 cycles at C/5	[38]
	Not provided	80:10:10	2.5–4.25	54% after 100 cycles at C/10	[39]
	2–3	80:10:10	2.7–4.3	98% retention after 50 cycles at 1 C	This work

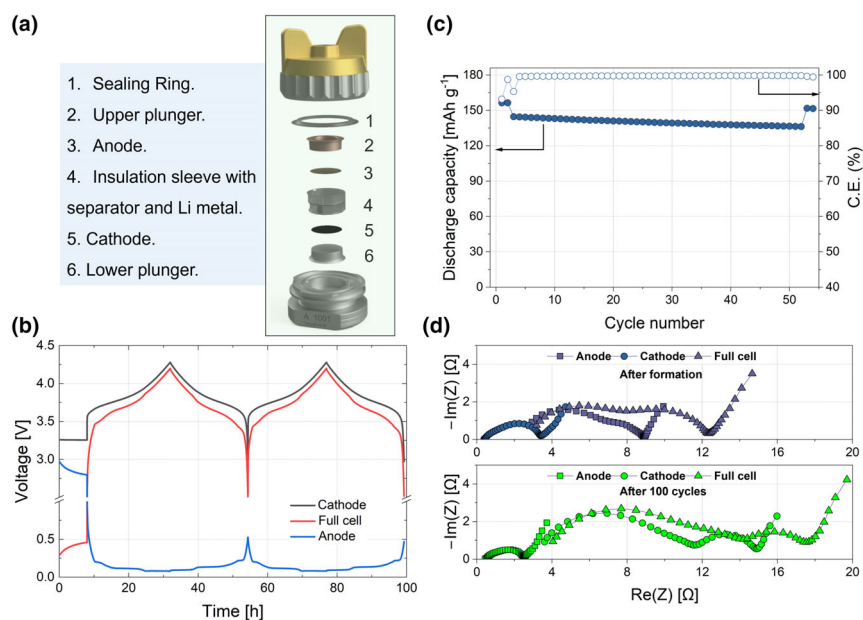


Figure 4. a) 3E cell configuration. b) Voltage profiles from 3E cell during the first formation cycle at C/20. c) Cycle life. EIS data d) after formation and 50 cycles. EIS is measured at 3.8 V of full cell voltage.

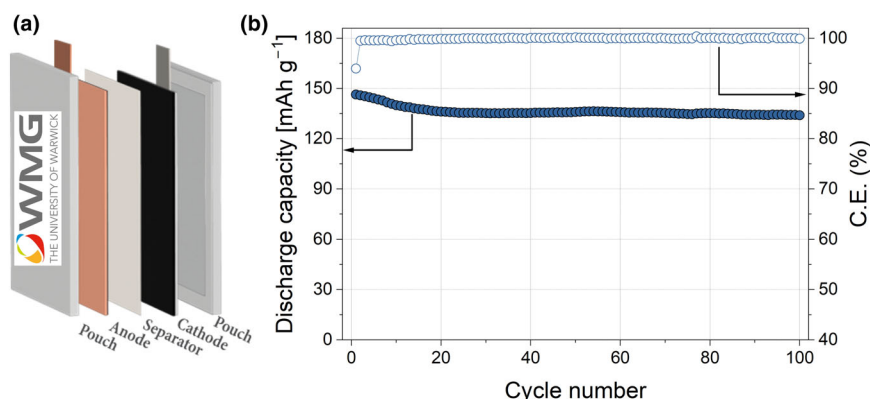


Figure 5. a) Pouch cell configuration. b) Cycle life of NMC111/graphite SLP cycled between 2.5 and 4.2 V at C/3.

Li-ion battery cathodes.^[42] The observed rate performance was acceptable considering the high mass loading of the electrodes, that is, tailored for energy dense applications.

Employing a three-electrode (3E) cell configuration (Figure 4a), which includes a Li reference electrode, allows observation of both cathode and anode potentials and differentiates between their impedance contributions. Compared with half cells, 3E cells eliminate the polarization contribution from the chosen counter electrode, resulting in higher data accuracy. The cathode potential, anode potential, and full cell voltage profiles for the first cycle are shown in Figure 4b. Figure 4c shows two formation cycles at C/20, followed by 50 cycles at C/3, and two diagnostic cycles at C/20, of a 3E cell assembled using brine-NMC and graphite. The discharge-specific capacities were 156.4 and 156.3 mAh g⁻¹, respectively, during the first two formation cycles, with CEs of 93.17% and 98.74%. The initial discharge capacity at C/3

was 144 mAh g⁻¹, and after 50 cycles, the capacity retention was 94.2%, implying good electrochemical behavior. Electrochemical impedance spectroscopy (EIS) measurements before and after cycling revealed that the anode impedance was slightly lowered, whereas the cathode impedance was increased (Figure 4d). We performed EIS fitting on anode spectra (Figure S6, Table S2, Supporting Information). The results identified that the solid electrolyte interphase (SEI) resistance (R_{SEI}) increased over cycling, which may be attributed to transition metal (TM) dissolution and deposition on the anode interface, as reported in the literature.^[43,44] However, the slight reduction in overall impedance was due to the lowering of charge transfer resistance (R_{CT}), which can be attributed to enhanced particle wetting caused by aging alongside volumetric changes in the graphite electrode during cycling.^[45] The cathode impedance increase could be attributed to surface film formation, material degradation, and/or dissolution of the TMs.^[46,47]

For a more practical evaluation of electrochemical behavior relevant for commercial applications, and to further extend the validation of the brine-sourced Li₂CO₃, 5 cm × 7 cm (A7)-sized single-layer pouch cells (SLPs) (Figure 5a) were built using brine-NMC111 and graphite electrodes. Pouch cells are employed in system applications because of their ability to maximize space utilization and their high active material packing efficiency, which offers high energy densities.^[48] In addition, the pouch cell format enables operando X-ray analysis of real, unmodified cells to verify cathode lithiation mechanisms. Figure S7, Supporting Information shows the voltage profiles of the NMC111/graphite SLP. The first cycle discharge capacity of the SLP was 152 mAh g⁻¹ with a CE of 91.69%. Figure 5b illustrates the discharge-specific capacity as a function of the cycle number for the SLP at a C/3 rate. After 100 cycles, the discharge capacity retention was

92%. The higher capacity loss here when compared to that of coin cells is reflective of the leaner electrolyte environment, confirming the importance of testing in larger format cells. The 8% loss in capacity was further investigated through operando XRD and postmortem analysis of the electrodes as detailed in later sections.

Operando XRD measurements are essential for studying the dynamics of the crystal structure of the cathode during lithium-ion intercalation and deintercalation, offering real-time insights into the structural evolution. In this study, operando XRD was performed on the NMC111/graphite SLP cell previously used for electrochemical cycling, without any compromise to the cell format. While previous studies have often employed coin cells^[49,50] or short-duration operando XRD experiments,^[51] our work extends this by monitoring the performance of NMC111/graphite SLPs over prolonged cycling. Figure 6a,b presents the XRD data collected during cycles 1 and 101,

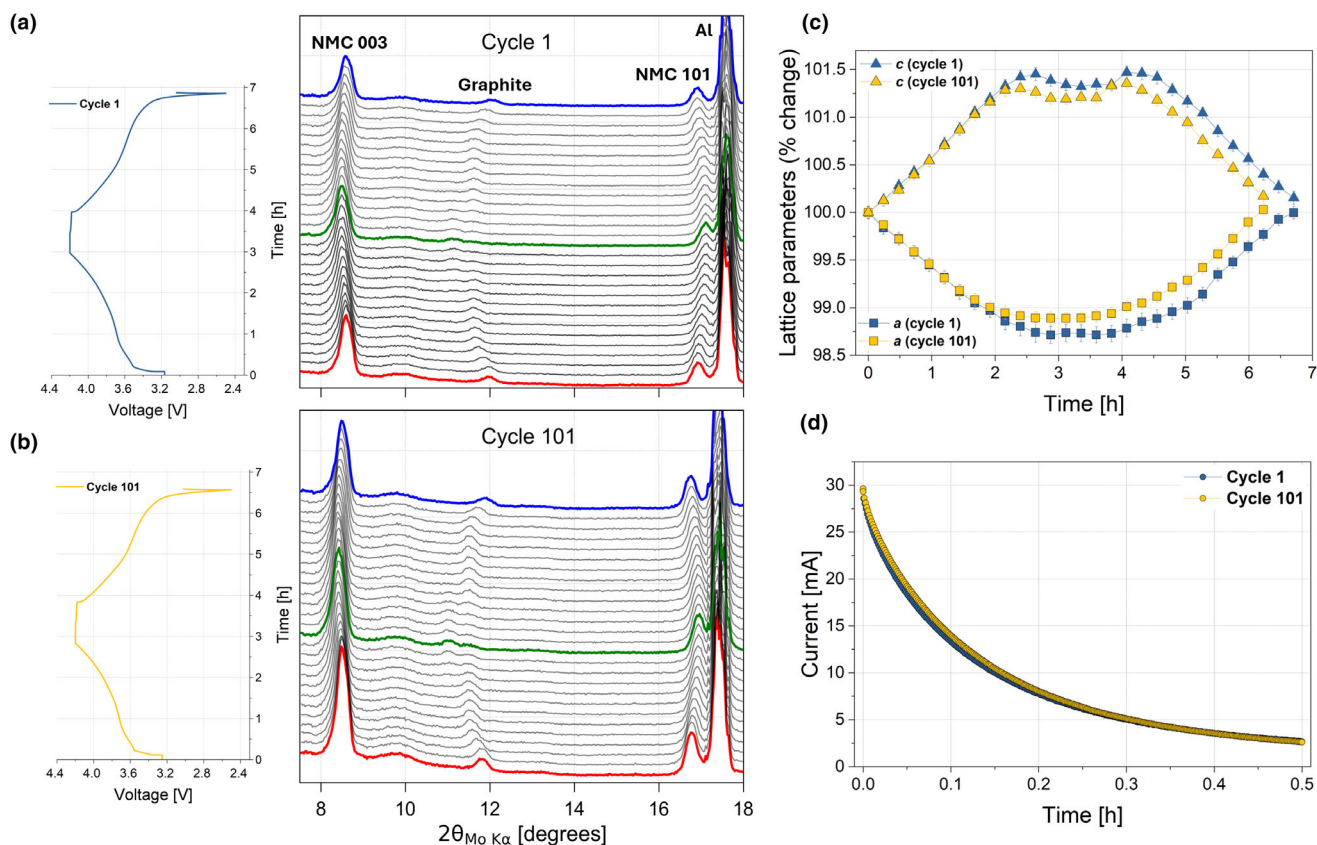


Figure 6. Operando XRD data (red: at OCV; green: at top of charge; blue: at discharge state) along with the voltage versus time profiles from a) cycle 1 and b) cycle 101. c) The evolution of *a*- and *c*-lattice parameters calculated from the sequential Pawley fitting of operando XRD data. d) The evolution of current during the CV step at 4.2 V of operando electrochemical cycling.

along with the corresponding voltage versus time profiles. The XRD data, recorded in the angular range (2θ) of 7.5° – 18.5° , show the (003) and (101) peaks from the NMC111 phase and the (002) and (111) peaks from the graphite and Al phases, respectively. During the charge (delithiation) of cycle 1, the (003) peak shifted to lower angles, indicating an increase in the interlayer spacing of the layered structure. This expansion is primarily due to the weakening of the screening effect of Li^+ ions on the adjacent TM layers, resulting in increased repulsion between them.^[52] At the top of charge, the (003) peak does not exhibit an abrupt shift to a higher angle, as typically observed in Ni-rich NMC cathodes; this is attributed to the so-called “*c*-lattice collapse”.^[53] The absence of lattice collapse in NMC111 is likely due to the relatively lower degree of delithiation within the applied voltage window (2.5–4.2 V). The (101) peak, associated with the *a*-*b* plane, continuously shifts to higher angles throughout charging, suggesting progressive contraction of the *a*-*b* plane as a response to lithium deintercalation. Upon discharge (lithiation), both the (003) and (101) peaks returned to their original positions, demonstrating the reversibility of structural evolution in NMC111. During cycle 101, the shift of the (003) peak was less pronounced, indicating a smaller degree of (de)lithiation, which can be attributed to the loss of Li inventory over 100 cycles.

Figure 6c illustrates the evolution of lattice parameters (*a* and *c*) and the corresponding unit cell volume during operando electrochemical

cycling. These parameters, derived from sequential Pawley fitting of raw operando XRD data, are presented as percentage changes to provide better insights into the structural evolution of NMC111. During charging, the *c*-lattice, which reflects the degree of (de)lithiation, increased as the voltage approached 4.2 V, followed by a slight dip at the top of the charge. This behavior aligns well with the evolution of the (003) peak. Meanwhile, the *a*-lattice, which mirrors the (101) peak and is associated with the *a*-*b* plane, continuously decreased until the top of the charge. During discharge, both the *a*- and *c*-lattices reverted to their original values, confirming the reversibility of the structural evolution of NMC111. After 100 cycles, the overall trend in lattice parameter evolution remained consistent, although the percentage increase in the *c*-lattice and the percentage decrease in the *a*-lattice were slightly reduced. This small percentage change in lattice parameters translates into a smaller percentage change in unit cell volume after 100 cycles, indicating the loss of lithium inventory.

To assess the impact of Li inventory loss on electrode kinetics, the current evolution (*I*) during the CV hold (at 4.2 V for 30 min) of the operando cycles was compared (Figure 6d). A similar current evolution suggests that Li^+ ion kinetics remain unaffected. The upper cutoff voltage (4.2 V) used in this study is significantly lower than the reported oxygen-loss threshold (4.6 V vs Li/Li^+) for NMC111, suggesting no surface layer reconstruction (e.g., rock salt layer with low Li^+ diffusion kinetics) occurs,^[54] thus preserving the kinetics despite the Li inventory loss.

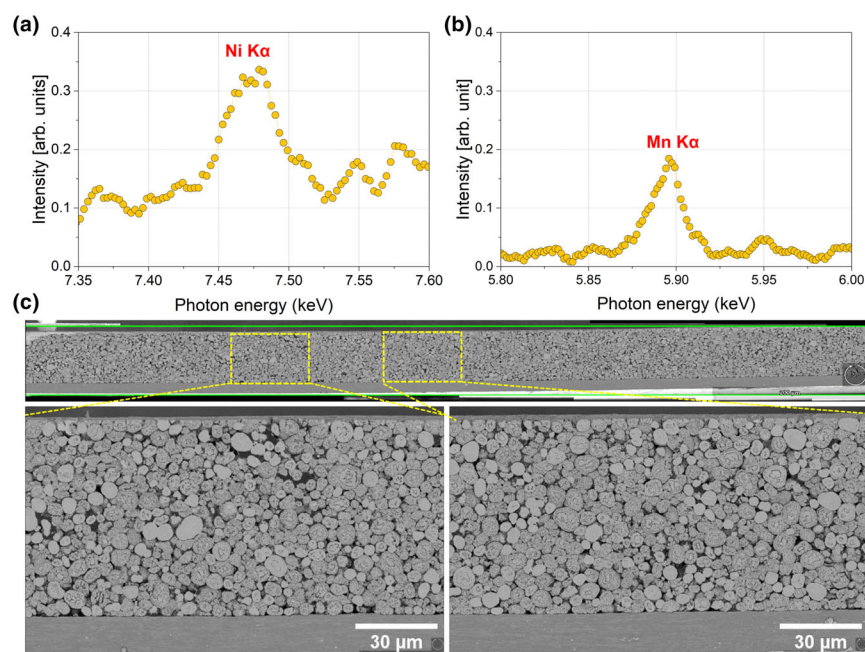


Figure 7. a) XRF measurements on the graphite electrodes centered on the a) Ni K α and b) Mn K α emission energy region to inspect transition metal dissolution. c) Cross-sectional SEM images of the cathode harvested from the NMC111/graphite SLP cell after cycling.

In addition to tracking the evolution of the (003) and (101) peaks of NMC111, the SLP format offers the advantage of simultaneously monitoring the (002) graphite peak at 11.8° , which undergoes multiple staging processes during lithium (de)intercalation. During Li $^+$ intercalation (charging), the (002) peak shifted to lower angles, indicating an increase in the interlayer spacing of the graphite structure. Conversely, during Li $^+$ deintercalation (discharging), the (002) peak reverted to higher angles.

After cycling, the SLP was carefully disassembled, and the electrodes were retrieved for microscopic and compositional analyses. During cycling, TM ions dissolve and migrate through the separator, embedding themselves into the SEI of the anode. This process is a further potential degradation mechanism associated with NMC materials.^[55] XRF of the graphite electrode from the disassembled SLP revealed Mn and Ni dissolution of 94.3 and 53.5 ppm, respectively (Figure 7a,b). For comparison, XRF measurements of the fresh graphite anode and a bare copper foil were conducted (Figure S8a,b, Supporting Information) to identify possible contamination. As shown in Figure S8c–e, Supporting Information, no Mn, Co, or Ni signals were detected in the fresh graphite, while the cycled anode clearly exhibited these elements. Also, XRF analysis of the bare copper foil revealed no detectable Mn, Co, or Ni signals, confirming that the observed TM presence is due to cycling rather than contamination (Figure S8c–e, Supporting Information). The deposition of TMs into the SEI layer leads to the trapping of Li $^+$ ions, resulting in the depletion of cyclable lithium.^[56–58] Therefore, the capacity fading over 100 cycles can be attributed to the loss of active lithium. No bulk phase changes occur in NMC111 during the 2.5–4.2 V window; however, this lithium inventory loss may influence the lattice parameters a and c , as observed in operando measurements. The SEM images of the cycled cell indicated no visible cracking of the cathode particle after 100 cycles (Figure 7c). Therefore, the performance fading of NMC111 cannot be attributed to the cracking

phenomenon. Finally, Figure S9, Supporting Information shows the Nyquist plot of the SLP after formation and 100 cycles. The 3E cell EIS data confirmed that the increase in total cell impedance can be ascribed to the cathode. Hence, the growth of an additional semi-circle after cycling in the case of SLP can be attributed to the dissolution of TMs, which can increase the interfacial impedance.^[59]

3. Conclusion

Li $_2$ CO $_3$ derived from brine beneath the Salar de Uyuni in Bolivia was successfully purified to battery-grade quality and validated as a suitable lithium source for the synthesis of NMC111 cathode material. The electrochemical performance of the synthesized NMC111 was evaluated using SLP and 3E cells under commercially relevant mass loadings to further validate the electrochemical quality of Li $_2$ CO $_3$ and its potential for battery applications. The 3E and SLP cells confirmed the good cycling stability of NMC111 material. The scale-up of synthesized material to SLPs provided reliable results relevant to real-world battery performance, in contrast to conventional half-coin cells and electrodes with low mass loading. This study bridges the entire process from raw material extraction to large-format cell evaluation, offering a comprehensive assessment of the potential of Bolivia's Salar de Uyuni as a scalable and sustainable source of lithium for the global battery market. Future research will involve assessing cycle life at high voltages (≥ 4.4 V vs graphite) and evaluating long-term cycling behavior. Additionally, synthesizing Li[Ni $_{0.6}$ Mn $_{0.2}$ Co $_{0.2}$]O $_2$, LiMn $_2$ O $_4$, or LiFePO $_4$ using Li $_2$ CO $_3$, and evaluating their electrochemical performance in large-format cells, will further validate the quality and applicability of brine-sourced Li $_2$ CO $_3$ for other cathode materials.

4. Experimental Section

Li $_2$ CO $_3$ extraction and purification: Li $_2$ CO $_3$ was obtained from the Salar de Uyuni, Bolivia. Brines beneath the Salar were pumped into evaporation ponds and allowed to evaporate water until the concentration of lithium in the brines reached approximately 5%. After the evaporation process, NaCl and other salts were removed. Subsequently, several chemical processes were applied in a Li $_2$ CO $_3$ plant to remove Mg, Ca, B, and other impurities. In the last step, sodium carbonate was used to precipitate Li $_2$ CO $_3$, leading to a technical-grade product.

The purification of Li $_2$ CO $_3$ to battery grade began with the preparation of raw materials by sieving. Then, bicarbonation was performed by dissolving technical-grade Li $_2$ CO $_3$ with carbon dioxide and deionized water to obtain a lithium bicarbonate solution, which was filtered to remove undissolved solids. Subsequently, EDTA-2Na was added to prevent the crystallization of magnesium and calcium carbonate.

The lithium bicarbonate solution was then heated to 90°C to evaporate water and form Li $_2$ CO $_3$ crystals. The product was filtered by centrifugation to separate the solid from any remaining liquid, yielding high-purity Li $_2$ CO $_3$. The product was washed at 70°C to remove soluble compounds, dried at 100°C , and finally micronized. Consequently, a “battery-grade” (min. 99.5% purity) material was obtained for cathode synthesis.

NMC111 synthesis: The cathode material was synthesized using a classical two-step process as follows.

Synthesis of carbonate precursor: In the first stage, a co-precipitation method was employed to synthesize an NMC-carbonate precursor. Stoichiometric amounts of $\text{NiSO}_4 \cdot 6\text{H}_2\text{O}$, $\text{CoSO}_4 \cdot 7\text{H}_2\text{O}$, and $\text{MnSO}_4 \cdot \text{H}_2\text{O}$ were dissolved in deionized H_2O to prepare a 2.5 M solution. Na_2CO_3 was dissolved in DI H_2O to form a solution with a concentration of 2.5 M. Both solutions were simultaneously introduced into a continuously stirred tank reactor, fully automated, at a flow rate of approximately 30 mL min^{-1} , while NH_4OH was incrementally added to maintain a stable pH. The reaction was carried out under controlled conditions at 50°C , with the reactor maintained at a stirring speed of 180 RPM to ensure homogeneity. After the complete addition of the reactants into the reactor, an additional reaction time (i.e., maturation process) of 30 min was used. Finally, the obtained carbonate precipitate was separated, washed, and dried at 60°C in an oven.

Synthesis of cathode material: The second step in the synthesis of cathode material involves a conventional solid-state reaction. The carbonate precursor was thoroughly mixed with battery-grade lithium carbonate in stoichiometric proportions, with an additional 15% excess lithium to compensate for losses due to sublimation during the calcination process. The mixture was calcined at 900°C for 12 h. Subsequently, the material was allowed to cool naturally overnight to room temperature. A similar procedure was carried out utilizing commercially obtained Li_2CO_3 to produce a baseline NMC111 material.

Material characterization: Powder XRD was performed using a Rigaku X-ray diffractometer operating at 40 kV and 15 mA, with $\text{Cu-K}\alpha$ radiation (1.5406 \AA). TOPAS academic software was used to perform the Rietveld refinement of powder XRD data. The crystallographic information of the input structural model for Rietveld refinement was obtained from the reference.^[60] The 6-coefficient polynomial function was used to determine the XRD background, and the error in the sample position was corrected by refining the sample displacement parameter. XRD peaks corresponding to the NMC111 phase were modeled using the Thompson–Cox–Hastings pseudo-Voigt peak shape function, and the asymmetry caused by the instrumental axial divergence was corrected by the Simple_Axial_Model. Scale factor was used to scale the calculated intensity during the refinement. Lattice parameters such as $a = b$, c , and the oxygen positions were refined. Li/Ni interlayer intermixing was determined from the occupancies of Li present in the Ni (TM) layer and the equivalent amount of Ni present in the Li layer. The occupancies of Mn and Co atoms were kept fixed at 1/3 each, and for oxygen, the occupancy was set at 1.0. Reliability parameters such as Rwp and goodness of fit (GoF) were used to evaluate the quality of fit.

The cross-section of cathode was prepared using a Hitachi IM4000Plus Ar ion milling system. Ion milling was carried out with an air protection unit to prepare the cross-section of the cycled electrodes in order to prevent moisture contamination of the sample. The cross-section was carried out at 6 kV for 2.5 hour with a 40° rocking stage. Surface and cross-sectional scanning electron microscopy (SEM) images were obtained by transferring the milled sample to a Thermo Fisher Scientific Scios Dualbeam scanning electron/focused ion beam microscope via a CleanConnect inert gas transfer system.^[61] Imaging was performed using an accelerating voltage of 2 kV and a beam current of 0.8 nA. Wide-area SEM montage images were acquired using Thermo Fisher Scientific Map Software and stitched together afterwards in order to investigate the cross-sectional cathode. Energy-dispersive X-ray spectroscopy (EDS) was performed with an accelerating voltage of 20 kV and a beam current of 1.6 nA using AZtec software (Oxford Instruments, UK). Wavelength-dispersive XRF (WD-XRF) spectroscopy was performed at the University of Warwick X-Ray Diffraction Research Technology Platform (RTP) using a Rigaku Primus IV system, which is equipped with a 4 kW Rh tube. Solid samples were analyzed under a 20 mm mask, using an “EZ Scan” protocol, which conducts an element sweep from B-U. The results are reported as mass % for major components and in ppm for trace elements, with a relative error of about 5% between samples. The particle size distribution was determined using a Malvern Mastersizer 3000 instrument with deionized water as the dispersing agent. The purity was determined using an atomic absorption spectrophotometer (Perkin Elmer, AAnalyst 200).

Electrode preparation and electrochemical characterization: The cathode electrode composition was prepared by blending NMC111, Super P, and PVDF in a 95.5:2.25 (wt.%) ratio in N-methyl-2-pyrrolidone. The slurry was coated onto an aluminium foil using a drawdown coater. The mass loading of the electrodes was

18 mg cm^{-2} , and the electrodes were calendered to achieve a density of 3.0 g cm^{-3} . The graphite electrode was composed of 95.25 wt% graphite, 2.25 wt% carbon black, and 2.5 wt% CMC/SBR. The mass loading of the graphite electrodes was 9.3 mg cm^{-2} . Anode electrodes were calendered to a density of 1.23 g cm^{-3} . The areal capacity ratio (N/P) of electrodes was 1.2, balanced to an upper cutoff voltage of 4.2 V. These electrodes were assembled in CR2032 half-coin, 3E, and single-layer pouch (SLP) cell formats. One molar lithium hexafluorophosphate (LiPF_6) in ethylene carbonate (EC) and ethyl methyl carbonate (EMC) (LP57) with 2% vinylene carbonate (VC) (Solvionic) was used as electrolyte. C-rate measurements were performed in a half-cell format at different C-rates (C/10, C/5, C/3, C/2, 1 C, and 2 C) using symmetric charge/discharge rates. The mass loading of the electrodes for cycle life testing using half-coin cells was $2\text{--}3 \text{ mg cm}^{-2}$ with 80:10:10 formulation, mimicking academic studies. Commercial NMC111 was purchased from AME Energy, China. The 3E cell studies were conducted using the PAT-EL-cells configuration with $120 \mu\text{L}$ of electrolyte. The charge–discharge test for all full cells was carried out between 2.5–4.2 V. For the 3E cells, formation cycles were carried out at a C-rate of C/20, while the cycling was carried out at C/3 using constant current (CC) charge and CC discharge modes.

SLP cells were built in WMG in a dry room (dew point of -45°C to -60°C) and filled with 1 g of electrolyte. The cells had a capacity of 80 mAh with an areal capacity of approximately 2.5 mAh cm^{-2} . Two formation cycles were carried out at C/20 at 40°C , followed by cycling at C/3 for 100 cycles at 25°C using CC and constant voltage (CV) charge (CV to C/30) and CC discharge modes. Potentiostatic electrochemical impedance spectroscopy (EIS) measurements were performed using a VMP3 potentiostat (BioLogic). The measurements were performed at 25°C from 100 kHz to 10 mHz with an amplitude of 10 mV. EIS measurements were performed at 3.8 V.

After cycling, the pouch cells were discharged to 2.5 V before being disassembled in an Ar-filled glove box (MBraun , $\text{O}_2 < 1 \text{ ppm}$, $\text{H}_2\text{O} < 1 \text{ ppm}$). The electrodes were then rinsed with dimethyl carbonate (DMC) (anhydrous min. 99% purity, Sigma Aldrich) to remove residual electrolyte.

Operando XRD measurements: Galvanostatic electrochemical cycling during the operando XRD measurements was performed at room temperature using a Biologic SP150 potentiostat. The cycling rate was maintained at C/3, with an intermediate CV hold at 4.2 V, and a rest step, each lasting 30 min between charge and discharge. Operando XRD data for the pouch cells were collected using a Malvern Panalytical Empyrean diffractometer operating at 60 kV and 40 mA, utilizing $\text{Mo-K}\alpha$ radiation ($K\alpha_1 = 0.709319 \text{ \AA}$, $K\alpha_2 = 0.713609 \text{ \AA}$). Data collection was conducted in transmission mode with the pouch cell mounted on the XYZ sample stage. The 2θ range spanned from 7.5° to 18° , with each scan taking approximately 15 min.

Sequential Pawley refinement of the operando XRD data was performed using Topas Academic software (version 7). Both the NMC111 and Al phases were included in the fitting process. The NMC111 phase was modeled using a rhombohedral unit cell with space group $R\bar{3}m$, whereas the Al phase was represented by a cubic unit cell with space group $Fm\bar{3}m$. The refinement incorporated the (003) and (101) reflections from the NMC111 phase and the (111) reflection from Al phase.

Acknowledgements

The authors would also like to acknowledge the funding from FCDO, UK. The British Embassy in La Paz–Bolivia is acknowledged for its kind collaboration in the logistics and communication exchange. The authors would like to acknowledge Frederick Taylor-Cross for his help in creating the coin, 3E, and SLP configuration images.

Conflict of Interest

The authors declare no conflict of interest.

Supporting Information

Supporting Information is available from the Wiley Online Library or from the author.

Keywords

brine, lithium carbonate, Salar de Uyuni, single-layer pouch cells, three-electrode cells

Received: December 20, 2024

Revised: April 30, 2025

Published online: May 12, 2025

- [1] J. Xie, Y.-C. Lu, *Nat. Commun.* **2020**, 11, 2499.
- [2] European Commission, Critical Raw Materials, https://single-market-economy.ec.europa.eu/sectors/raw-materials/areas-specific-interest/critical-raw-materials_en#fifth-list-2023-of-critical-raw-materials-for-the-eu, (accessed: October 2024).
- [3] U.S. Department of Energy, Critical Materials Assessment, https://www.energy.gov/sites/default/files/2023-07/doe-critical-material-assessment_07312023.pdf, (accessed: October 2024).
- [4] M. L. Vera, W. R. Torres, C. I. Galli, A. Chagnes, V. Flexer, *Nat. Rev. Earth Environ.* **2023**, 4, 149.
- [5] International Energy Agency, The Role of Critical Minerals in Clean Energy Transitions, <https://iea.blob.core.windows.net/assets/ffd2a83b-8c30-4e9d-980a-52b6d9a86fdc/TheRoleofCriticalMineralsinCleanEnergyTransitions.pdf>, (accessed: October 2024).
- [6] N. Sharmili, R. Nagi, P. Wang, *J. Energy Storage* **2023**, 68, 107622.
- [7] J. C. Kelly, M. Wang, Q. Dai, O. Winjobi, *Resour. Conserv. Recycl.* **2021**, 174, 105762.
- [8] T.-M. Gao, N. Fan, W. Chen, T. Dai, *China Geol.* **2023**, 6, 137.
- [9] G. Haferburg, J. A. D. Gröning, N. Schmidt, N.-A. Kummer, J. C. Erquicia, M. Schlömann, *Microbiological Research* **2017**, DOI: [10.1016/j.micres.2017.02.007](https://doi.org/10.1016/j.micres.2017.02.007).
- [10] Lithium, <https://pubs.usgs.gov/periodicals/mcs2024/mcs2024-lithium.pdf>, (accessed: October 2024).
- [11] G. E. Ericksen, J. D. Vine, A. Raul Ballón, *Energy* **1978**, 3, 355.
- [12] J. W. An, D. J. Kang, K. T. Tran, M. J. Kim, T. Lim, T. Tran, *Hydrometallurgy* **2012**, 64, 117.
- [13] Z. Xu, H. Zhang, R. Wang, W. Gui, G. Liu, Y. Yang, *Ind. Eng. Chem. Res.* **2014**, 53, 16502.
- [14] T. Lestariningsih, A. Subhan, Q. Sabrina, C. R. Ratri, L. H. Lalasari, S. Priyono, A. Rifai, *AIP Conf. Proc.* **2024**, 3003, 020038.
- [15] D. Thompson, C. Hyde, J. M. Hartley, A. P. Abbott, P. A. Anderson, G. D. J. Harper, *Resour. Conserv. Recycl.* **2021**, 175, 105741.
- [16] Z. Wang, J. Yuan, X. Zhu, H. Wang, L. Huang, Y. Wang, S. Xu, *J. Energy Chem.* **2021**, 55, 484.
- [17] X. Han, Q. Meng, T. Sun, J. Sun, *J. Power Sources* **2010**, 195, 3047.
- [18] R. Jung, R. Morasch, P. Karayaylali, K. Phillips, F. Maglia, C. Stinner, Y. Shao-Horn, H. A. Gasteiger, *J. Electrochem. Soc.* **2018**, 165, A132.
- [19] L. Ma, M. Nie, J. Xia, J. R. Dahn, *J. Power Sources* **2016**, 327, 145.
- [20] R. Santhanam, B. Rambabu, *J. Power Sources* **2010**, 195, 4313.
- [21] A. Smith, P. Stüble, L. Leuthner, A. Hofmann, F. Jeschull, L. Mereacre, *Batteries Supercaps* **2023**, 6, e202300080.
- [22] N. Delpuech, N. Dupre, P. Moreau, J.-S. Bridel, J. Gaubicher, B. Lestriez, D. Guyomard, *ChemSusChem* **2016**, 9, 841.
- [23] C. Peng, F. Liu, Z. Wang, B. P. Wilson, M. Lundström, *J. Power Sources* **2019**, 415, 179.
- [24] A. Higuchi, N. Ankei, S. Nishihama, K. Yoshizuka, *JOM* **2016**, 68, 2624.
- [25] J. Hou, X. Ma, J. Fu, P. Vanaphuti, Z. Yao, Y. Liu, Z. Yang, Y. Wang, *Green Chem.* **2022**, 24, 7049.
- [26] T. Ohzuku, Y. Makimura, *Chem. Lett.* **2003**, 30, 642.
- [27] F. Omenya, N. A. Chernova, H. Zhou, C. Siu, M. S. Whittingham, ECS Meeting Abstracts 2018, MA2018-01, 531.
- [28] S.-Y. Kim, Y.-J. Yang, E. G. Lee, M.-S. Kim, K.-J. Go, M. Kim, G.-Y. Kim, S. Lee, C. Jo, S. Choi, S.-Y. Choi, *Chem. Eng. J.* **2024**, 482, 148869.
- [29] F. Du, X. Zhang, Y. Wang, L. Ding, P. Zhang, L. Liu, D. Wang, J. Man, Y. Chen, Y. Li, *J. Energy Chem.* **2024**, 97, 20.
- [30] H. Yu, Y. Qian, M. Otani, D. Tang, S. Guo, Y. Zhu, H. Zhou, *Energy Environ. Sci.* **2014**, 7, 1068.
- [31] X. Tan, W. Peng, M. Wang, G. Luo, Z. Wang, G. Yan, H. Guo, Q. Li, J. Wang, *Prog. Nat. Sci. Mater. Int.* **2023**, 33, 108.
- [32] M. Wang, Y. Chen, F. Wu, Y. Su, L. Chen, D. Wang, *Electrochim. Acta* **2010**, 55, 8815.
- [33] N. Anansuksawat, T. Sangsanit, S. Prempluem, K. Homlamai, W. Tejangkura, M. Sawangphruk, *Chem. Sci.* **2024**, 15, 2026.
- [34] M.-H. Lee, Y.-J. Kang, S.-T. Myung, Y.-K. Sun, *Electrochim. Acta* **2004**, 50, 939.
- [35] R. Dominko, M. Gaberscek, J. Drogenik, M. Bele, S. Pejovnik, J. Jamnik, *J. Power Sources* **2003**, 119–121, 770.
- [36] J. H. Mugumya, M. L. Rasche, R. F. Rafferty, A. Patel, S. Mallick, M. Mou, J. A. Bobb, R. B. Gupta, M. Jiang, *Energy Fuel* **2022**, 36, 12261.
- [37] W. Hua, W. Liu, M. Chen, S. Indris, Z. Zheng, X. Guo, M. Bruns, T.-H. Wu, Y. Chen, B. Zhong, S. Chou, Y.-M. Kang, H. Ehrenberg, *Electrochim. Acta* **2017**, 232, 123.
- [38] S. Zhang, C. Deng, S. Y. Yang, H. Niu, *J. Alloys Compd.* **2009**, 484, 519.
- [39] L. Yv, J. Wang, X. Li, L. Dai, Z. Shao, *Ionics* **2021**, 27, 3769.
- [40] V. Gupta, M. Appleberry, W. Li, Z. Chen, *Next Energy* **2024**, 2, 100091.
- [41] Y. Kuang, C. Chen, D. Kirsch, L. Hu, *Adv. Energy Mater.* **2019**, 9, 1901457.
- [42] Y. Chen, J. Key, K. O'Regan, T. Song, Y. Han, E. Kendrick, *Chem. Eng. J.* **2022**, 450, 138275.
- [43] E. Adhitama, F. Demelash, T. Brake, A. Arifiadi, M. Vahnstiege, A. Javed, M. Winter, S. Wiemers-Meyer, T. Placke, *Adv. Energy Mater.* **2024**, 14, 2303468.
- [44] T. Joshi, K. Eom, G. Yushin, T. F. Fuller, *J. Electrochem. Soc.* **2014**, 161, A1915.
- [45] E. M. C. Jones, Ö. Ö. Çapraz, S. R. White, N. R. Sottos, *J. Electrochem. Soc.* **2016**, 163, A1965.
- [46] E. Laakso, S. Efimova, M. Colalongo, P. Kauranen, K. Lahtinen, E. Napolitano, V. Ruiz, J. Moškon, M. Gabersček, J. Park, S. Seitz, T. Kallio, *J. Power Sources* **2024**, 599, 234159.
- [47] D. Aurbach, M. D. Levi, K. Gamulski, B. Markovsky, G. Salitra, E. Levi, U. Heider, L. Heider, R. Oesten, *J. Power Sources* **1999**, 81–82, 472.
- [48] S. Chen, C. Niu, H. Lee, Q. Li, L. Yu, W. Xu, J.-G. Zhang, E. J. Dufek, M. S. Whittingham, S. Meng, J. Xiao, J. Liu, *Joule* **2019**, 3, 1094.
- [49] A. V. Ivanishchev, I. A. Bobrikov, I. A. Ivanishcheva, O. Y. Ivanshina, *J. Electroanal. Chem.* **2018**, 821, 140.
- [50] A. P. Black, C. Escudero, F. Fauth, M. Fehse, G. Agostini, M. Reynaud, R. G. Houdeville, D. Chatzogiannakis, J. Orive, A. Ramo-Ilrurre, M. Casas-Cabanas, M. R. Palacin, *Chem. Mater.* **2024**, 36, 5596.
- [51] E. Hu, X. Wang, X. Yu, X.-Q. Yang, *Acc. Chem. Res.* **2018**, 51, 290.
- [52] A. O. Kondrakov, A. Schmidt, J. Xu, H. Geßwein, R. Mönig, P. Hartmann, H. Sommer, T. Brezesinski, J. Janek, *J. Phys. Chem. C* **2017**, 121, 3286.
- [53] A. S. Menon, N. Shah, J. A. Gott, E. Fiammegkou, M. J. W. Ogle, G. J. Páez Fajardo, N. Vaenas, I. Ellis, N. Ravichandran, P. Cloetens, D. Karpov, J. M. Warnett, P. Malliband, D. Walker, G. West, M. Loveridge, L. F. J. Piper, *PRX Energy* **2024**, 3, 013004.
- [54] W. M. Dose, I. Temprano, J. P. Allen, E. Björklund, C. A. O'Keefe, W. Li, B. L. Mehdi, R. S. Weatherup, M. F. L. De Volder, C. P. Grey, *ACS Appl. Mater. Interfaces* **2022**, 14, 13206.
- [55] Z. Ruff, C. Xu, C. P. Grey, *J. Electrochem. Soc.* **2021**, 168, 060518.
- [56] E. Björklund, C. Xu, W. M. Dose, C. G. Sole, P. K. Thakur, T.-L. Lee, M. F. L. De Volder, C. P. Grey, R. S. Weatherup, *Chem. Mater.* **2022**, 34, 2034.
- [57] J. A. Gilbert, I. A. Shkrob, D. P. Abraham, *J. Electrochem. Soc.* **2017**, 164, A389.
- [58] R. Jung, F. Linsenmann, R. Thomas, J. Wandt, S. Solchenbach, F. Maglia, C. Stinner, M. Tromp, H. A. Gasteiger, *J. Electrochem. Soc.* **2019**, 166, A378.
- [59] C. Zhan, T. Wu, J. Lu, K. Amine, *Energy Environ. Sci.* **2018**, 11, 243.
- [60] J. Xu, S.-L. Chou, Q.-f. Gu, H.-K. Liu, S.-X. Dou, *J. Power Sources* **2013**, 225, 172.
- [61] K. K. Neelisetty, J. Stetina, J. Vondruška, M. Trenz, T. Kazda, M. Hrouzek, P. Wandrol, *Microsc. Microanal.* **2021**, 27, 2508.